

Denoising of Dense Spatial Array Data Using the Curvelet Transform

Jia Zhang^{1,2} , Charles A. Langston³ , and Hongfeng Yang^{*1,2} 

ABSTRACT

To remove background noise from seismic data recorded by spatially dense arrays, we have developed a space-based denoising procedure using the discrete curvelet transform. Based on a detailed statistical characterization of noise coefficients through the empirical cumulative distribution function method within a pre-event time window, signal and noise can be separated effectively by nonlinear thresholding. After synthetic test, we applied this method on data from an industry 3D seismic experiment recorded at an array deployed near Utica, Ohio. The denoising results show good waveform consistency with a significantly enhanced signal-to-noise ratio. Our curvelet approach allows a more computationally efficient spatial-temporal localization analysis of seismic data than conventional curvelet techniques by avoiding the assumption of stationary Gaussian-distributed noise and can be implemented as a complement of time-domain wavelet methods with fewer frequency losses after denoising. This new method provides a fast and convenient way to recover signals from noisy recordings with dense 2D arrays, leading to a considerable improvement in data quality compared with conventional Fourier, wavelet, and curvelet methods. The partitioned seismic signals and noise would yield advanced earth structure imaging, small-event detection, ambient noise tomography, and others.

KEY POINTS

- We characterize the localization feature of noise and signal and develop a denoising method using curvelets.
- We present significant advances in noise reduction by curvelets in the spatial domain using dense arrays.
- Curvelets work well in seismic denoising and designating and complement time-domain wavelet methods.

[Supplemental Material](#)

INTRODUCTION

Seismic arrays are attaining denser spatial sampling as new array configurations are proposed and seismometers are improved (Mykkeltveit *et al.*, 1983). High spatial density array datasets with tens to hundreds of meters of interstation distance offer unprecedented opportunities for advancing Earth structure imaging and source physics studies. For example, Huang (2001) monitored the rupture propagation of the M_w 7.7 Chi-Chi, Taiwan, earthquake by analyzing stacked seismic waveforms from a dense array with a coverage of 30×10 km. Ben-Zion *et al.* (2015) imaged subsurface structure within the San Jacinto fault zone in southern California from a spatially dense nodal array composed of 1100 sensors in an ~ 600 m \times 600 m configuration, which improved our understanding of fault zone structure compared with previous small-aperture arrays (e.g., Yang and Zhu, 2010; Yang *et al.*, 2014).

Inbal *et al.* (2016) placed the seismicity identified by two dense arrays in Long Beach, southern California, including the 5200-seismometer 7 km \times 10 km Long Beach array and the 2600-sensor 5 km \times 5 km Rosecrans array to a localized zone embedded in the upper mantle. Yang, Duan, *et al.* (2020) derived high-resolution fault zone structure beneath the Chenghai fault, Yunnan, southwest China, using an 8-km-long array with an average interstation distance of 50 m based on which a number of new methods had been developed to image crustal fault zones (Jiang *et al.*, 2021; She *et al.*, 2022; Song and Yang, 2022). However, datasets acquired from dense array deployments are subject to contamination by unwanted noise, usually incoherent and random caused by ocean surf, wind, local traffic, or imbalance of geophone responses, among other natural and cultural sources (Yilmaz, 2001; Stutzmann *et al.*, 2012; Behm *et al.*, 2014). Distinguishing a desired signal from the noisy dataset remains a key problem in array seismology.

1. Shenzhen Research Institute, The Chinese University of Hong Kong, Shenzhen, China,  <https://orcid.org/0000-0002-7831-6561> (JZ);  <https://orcid.org/0000-0002-5925-6487> (HY); 2. Earth and Environmental Sciences Programme, Faculty of Science, The Chinese University of Hong Kong, Shatin, Hong Kong, China; 3. Center for Earthquake Research and Information, University of Memphis, Memphis, Tennessee, U.S.A.,  <https://orcid.org/0000-0002-2385-918X> (CAL)

*Corresponding author: hyang@cuhk.edu.hk

Cite this article as Zhang, J., C. A. Langston, and H. Yang (2024). Denoising of Dense Spatial Array Data Using the Curvelet Transform, *Bull. Seismol. Soc. Am.* **XX**, 1–16, doi: [10.1785/0120240030](https://doi.org/10.1785/0120240030)

© Seismological Society of America

Many techniques have been developed to reduce noise power in dense array recordings. Band-pass filtering has been routinely utilized to suppress noise by a roughly estimated frequency cutoff. Apparently, it is deficient in separating the signal and noise within the same frequency band (Douglas, 1997). Recently, a number of Fourier-based and wavelet-based transforms have been employed for data denoising by taking advantage of the sparse representation of seismic data through linear transformations. The power of these denoising techniques is realized by reducing the information of time series data through a transform followed by amplitude thresholds in the transformed domain based on the different distribution of noise and signal (Tang and Ma, 2010; Langston and Mousavi, 2019). For example, the $\tau-p$ method suppresses noise in the time-slowness domain by filtering and allows for efficient manifestation of the reflected phases (Turner, 1990; Basak et al., 2012). The wavelet transform utilizes various wavelet functions to represent the seismic data in a compact form and separate noise and signal through their different distribution on the wavelet scale-time plane (Gaci, 2013; Mousavi and Langston, 2016). Besides, the wavelet packet transform, which comprises a flexible subband architecture, allows a detailed decomposition of the signal in the time-frequency plane and has yielded success in detecting and differentiating seismic signals with the high-frequency transient components (Galiana-Merino et al., 2003). Recently, the S transform, as an extension of the continuous wavelet transform windowed by a Gaussian function (Stockwell et al., 1996), has been used for optimally denoising seismograms and extracting ground-motion signals to investigate the seismic response of soils and buildings (Parolai, 2009; Ditommaso et al., 2012).

The curvelet, or the “directional wavelet,” completes a multiscale, multidirectional representation of large data volumes with enhancing sparsity and outperforms Fourier series and wavelets with its property of capturing data “curvature” in space because of its curve-like construction (Candes and Demanet, 2003). Compared with wavelets, a curvelet has faster decay of coefficients near discontinuities (Candes and Demanet, 2005). Therefore, the curvelet transform has been widely employed in seismic data analysis, such as data denoising (Herrmann et al., 2008), wavefield reconstruction (Herrmann and Hennenfent, 2008), and wave propagation simulation (Sun et al., 2009). Most of the present curvelet denoising procedures focus on differing “continuity” of shot records and treat the noise as stationary and Gaussian distributed (Herrmann et al., 2008; Tang and Ma, 2010). Under such an assumption, a Gaussian criterion is then employed to remove the noise power by thresholding, retrieving the desired seismic signals (Herrmann et al., 2007). However, the spatio-temporal localization of a Gaussian noise in the curvelet domain has not yet been thoroughly studied, and the seismic signals could be recovered with erroneous amplitudes using Gaussian criteria (Langston and Mousavi, 2019).

In this study, we perform a detailed analysis of curvelet coefficient distribution of noise over lag time and use a straightforward idea that noise and signal from a dense array can be separated in space by thresholding. We assume that the background noise field is stationary but varies across sensor location. The curvelet transform is manipulated by taking individual snapshots at discrete time points and results in a 2D space-frequency mapping to improve resolution by dense spatial sampling. In the following, we first investigate the characteristic statistics of synthetic Gaussian noise and real noise data via the curvelet transform to examine the plausibility of Gaussian criterion for denoising. Based on the statistics of noise coefficients, the noise level is better estimated by fitting the data with empirical cumulative distribution functions (ECDFs) and then employed to denoise the raw data through nonlinear thresholding. In addition to synthetics, the new curvelet technique is applied to a dataset of two seismic events recorded by an industry array deployed near Utica, Ohio. The results illustrate that background noise can be significantly suppressed, and signals can be retrieved with high fidelity. Our denoising method offers an intuitive and unique way to separate noise and signal using dense 2D arrays.

METHODOLOGY

The 2D seismic wavefield record D , including the signal S contaminated by background noise N , can be generally modeled as follows:

$$D(\vec{x}, t) = S(\vec{x}, t) + N(\vec{x}, t), \quad (1)$$

in which \vec{x} denotes the position vector in 2D space and t represents time. We apply the curvelet transform in space so the wavefield for each snapshot will be mapped into orthogonal localized prototype waveforms at different scales, directions, and locations (Candes et al., 2006; Fig. 1). Because the curvelet transform is linear and Fourier based, the seismic wavefield at a certain time point $t = t_0$ obeys the following relationship after transformation:

$$C_{j,l,k}^{D^{t_0}} = C_{j,l,k}^{S^{t_0}} + C_{j,l,k}^{N^{t_0}}, \quad (2)$$

in which $C_{j,l,k}^{i_{th}^{t_0}} = \langle i_{th}(\vec{x}, t_0), \varphi_{j,l,k} \rangle$ represents the curvelet coefficient of the i_{th} component of the wavefield at a specific scale j , orientation l , and translation $k = (k_1, k_2) \in Z^2$. The coefficient is calculated through a scalar product of the arbitrary spatial function $i_{th}(\vec{x})$ recorded at time t_0 and the curvelet $\varphi_{j,l,k}$. Taking all the curvelet coefficients of seismic record D , signal S , and noise N in their chronological order for each curvelet parameter group (j, l, k) gives the time sequencing data $\{C_{j,l,k}^{D^{t_n}}\}$, $\{C_{j,l,k}^{S^{t_n}}\}$, and $\{C_{j,l,k}^{N^{t_n}}\}$, respectively, in which t_n denotes the time sample for index n .

Although the denoising procedure is performed for a 3D curvelet matrix by analyzing each (j, l, k) group per snapshot,

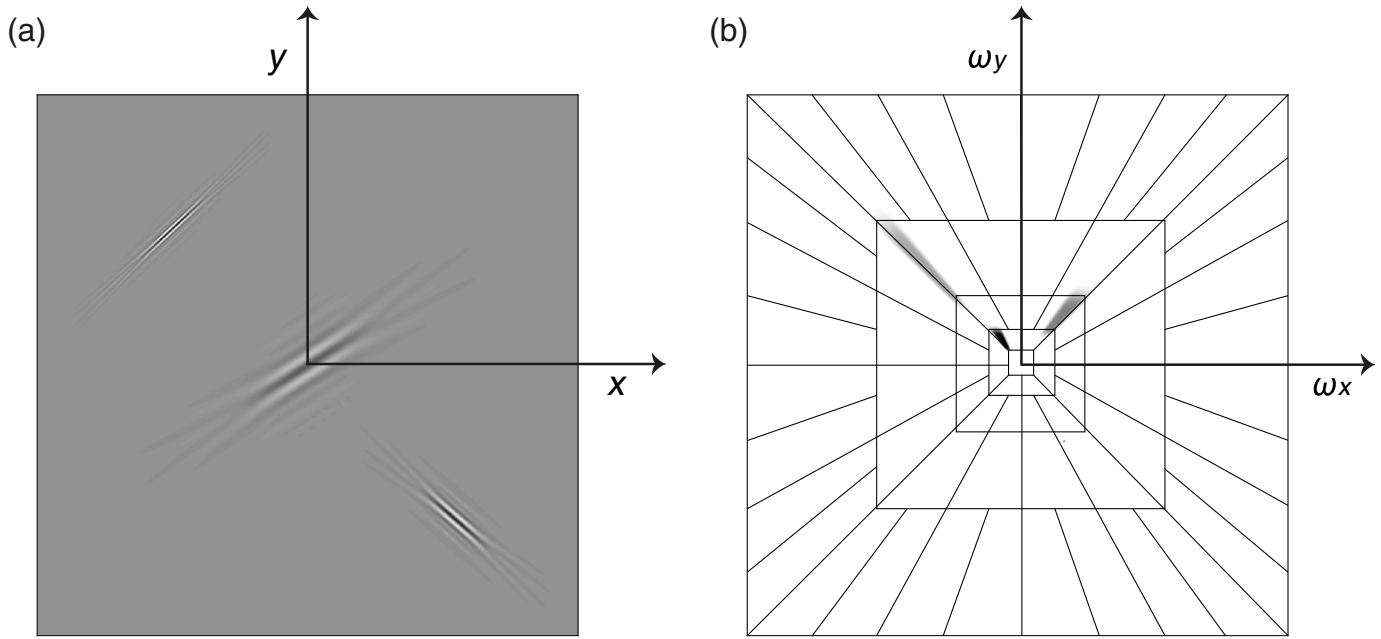


Figure 1. Curvelets at three different scales, directions, and locations are displayed both in the (a) spatial and (b) frequency domains. Note that the curvelet is localized within an angular wedged window and has a parabolic scaling of length \approx width² in the frequency domain.

a concatenation operation is conducted here to help understand how the curvelet coefficients are distributed over time for different (j, l, k) group. For a certain seismic station (or a fixed position in space), we flatten the 3D curvelet matrix into a 2D array by picking up all the curvelet coefficients at each scale and direction group (j, l) and rearranging them by different time points to eventually obtain an in situ “scalogram” (Fig. 2). It is not necessary to scan over the translation parameter k because for a fixed (j, l) group, the wavefield information is mostly enclosed by the curvelet closest to the station.

Eliminating the $\{C_{j,l,k}^{D^n}\}$ groups is the key to retrieving the desired signal $S(\vec{x}, t)$ from the observation $D(\vec{x}, t)$. Here, we adopt a widely used approach, thresholding, to suppress the noise level. Previous studies have demonstrated the effectiveness of thresholding (Candes *et al.*, 2006; Ma and Plonka, 2010; Naghizadeh and Sacchi, 2010). The central idea is to extract the signal-affiliated coefficients by removing an estimate of the noise coefficient from the entire sequence data $\{C_{j,l,k}^{D^n}\}$. A threshold function $T(\cdot)$ is determined in the curvelet domain at each (j, l, k) group by measuring the absolute value of the noise coefficients within a pre-event window. Then the signal coefficients $\{C_{j,l,k}^{S^n}\}$ can be recovered by various thresholding techniques (Weaver *et al.*, 1991; Li and Liang, 2012). Among these, nonlinear thresholding, including hard and soft thresholding, has been suggested to handle large seismic datasets in an explicit and effective way (Donoho and Johnstone, 1995). Normally, hard thresholding is performed by keeping all elements in the sequence $\{C_{j,l,k}^{D^n}\}$ if they are greater than a given threshold $\beta_{j,l,k}$ or otherwise setting to zero, which can be expressed by the following equation:

$$\tilde{C}_{j,l,k}^{D^n} = T(C_{j,l,k}^{D^n})^{\text{hard}} = \begin{cases} C_{j,l,k}^{D^n} & \text{if } |C_{j,l,k}^{D^n}| \geq \beta_{j,l,k} \\ 0 & \text{Otherwise} \end{cases} \quad (3)$$

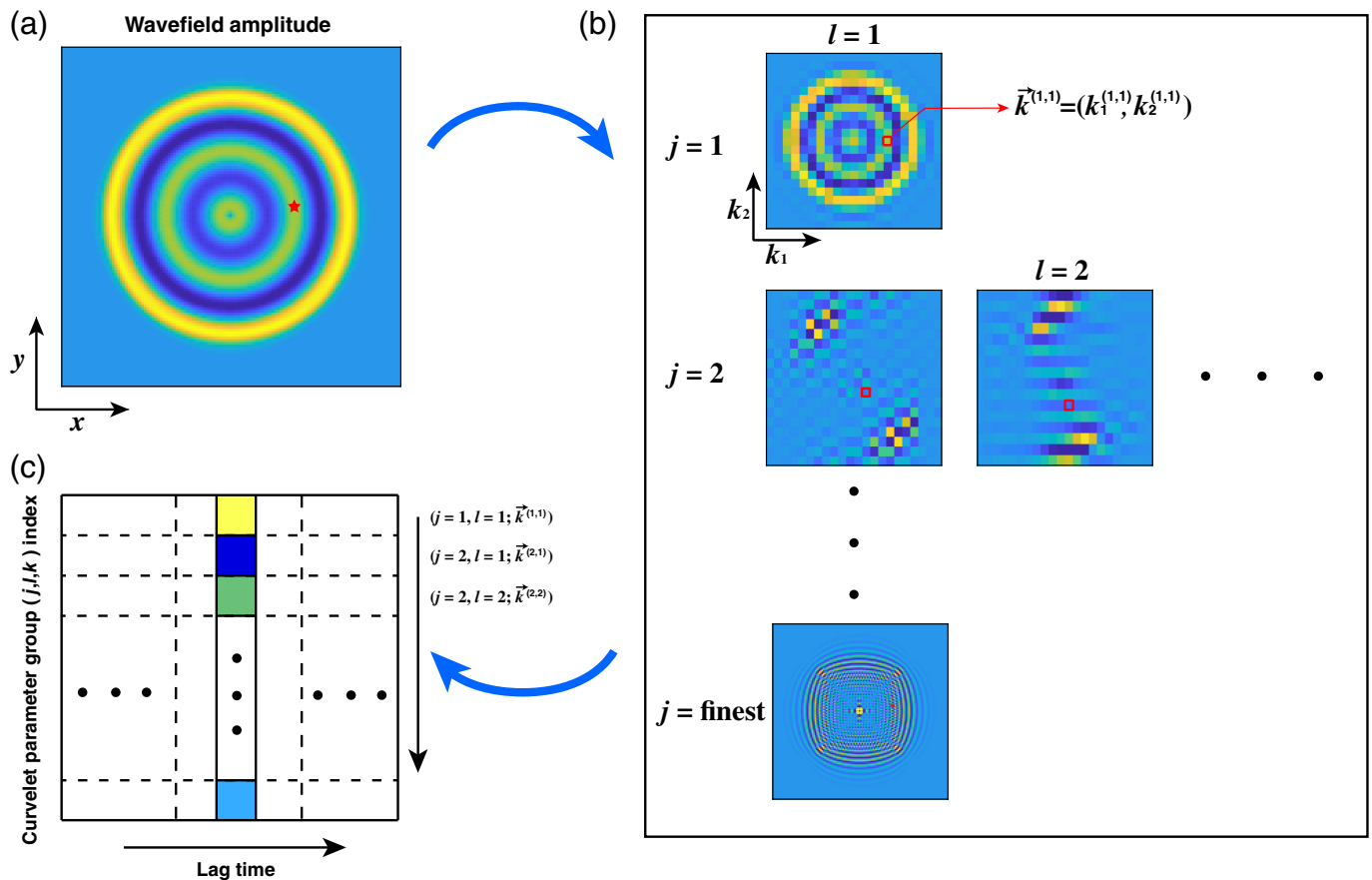
Note that the threshold $\beta_{j,l,k}$ is determined individually for each curvelet parameter group (j, l, k) . Alternatively, soft thresholding is done by shrinking all coefficients with magnitudes larger than the threshold by the inferred noise level $\beta_{j,l,k}$ and erasing all others:

$$\begin{aligned} \tilde{C}_{j,l,k}^{D^n} &= T(C_{j,l,k}^{D^n})^{\text{soft}} \\ &= \begin{cases} \text{sign}(C_{j,l,k}^{D^n})(|C_{j,l,k}^{D^n}| - \beta_{j,l,k}) & \text{if } |C_{j,l,k}^{D^n}| \geq \beta_{j,l,k} \\ 0 & \text{Otherwise} \end{cases}, \quad (4) \end{aligned}$$

in which

$$\text{sign}(C_{j,l,k}^{D^n}) = \frac{C_{j,l,k}^{D^n}}{|C_{j,l,k}^{D^n}|}. \quad (5)$$

Compared with hard thresholding, soft thresholding yields smoother signal estimates with fewer artifacts, which were introduced by the shrinkage operation (Chang *et al.*, 2000). However, a different choice of the threshold $\beta_{j,l,k}$ will directly affect denoising resolution. A detailed analysis of the statistical properties of noise coefficients is necessary for improving signal-to-noise ratio (SNR). In general, the noise field $N(\vec{x}, t)$ recorded on a seismic array is described as a superposition of uncorrelated waves propagating from all azimuths and distances (Harmon *et al.*, 2010) and originating from randomly distributed sources in space. As such, there is no specific propagation direction or dominant wavelength for the noise curvelet coefficients within a pre-event time window. The background noise may vary at different stations, usually



interpreted as a stationary and Gaussian time series (White, 1988; Bendat and Piersol, 2011; Zhong *et al.*, 2015). Therefore, the noise threshold by assuming Gaussian statistics is determined by the following equation:

$$\beta_{j,l,k} = \text{mean}(|C_{j,l,k}^{D^n}|) + c_0 \times \text{std}(|C_{j,l,k}^{D^n}|), \quad (6)$$

in which $\text{mean}(\cdot)$ represents the mean value and $\text{std}(\cdot)$ denotes the standard deviation of the magnitude of curvelet coefficients $\{|C_{j,l,k}^{D^n}|\}$ for a specific (j, l, k) group. A positive constant c_0 is used to quantify the threshold. For example, the signal can be obtained with a 99.7% confidence level by taking a choice of $c_0 = 3$ in an ideal Gaussian case (Starck *et al.*, 2010). A more flexible and data-dependent criterion called the “universal” threshold is suggested for the practical data (Donoho and Johnstone, 1994), which is given as follows:

$$c_0 = \sqrt{2 \log_{10} N}, \quad (7)$$

in which N is the total number of data samples. Normally, c_0 obtained from the universal threshold relationship exceeds a value of 3 when N is $> \sim 31,620$.

Nevertheless, the threshold $\beta_{j,l,k}$ is decided by taking the absolute value of the noise coefficients as in equation (6). This operation can alter the statistical distribution pattern of a Gaussian noise (Langston and Mousavi, 2019). To clarify

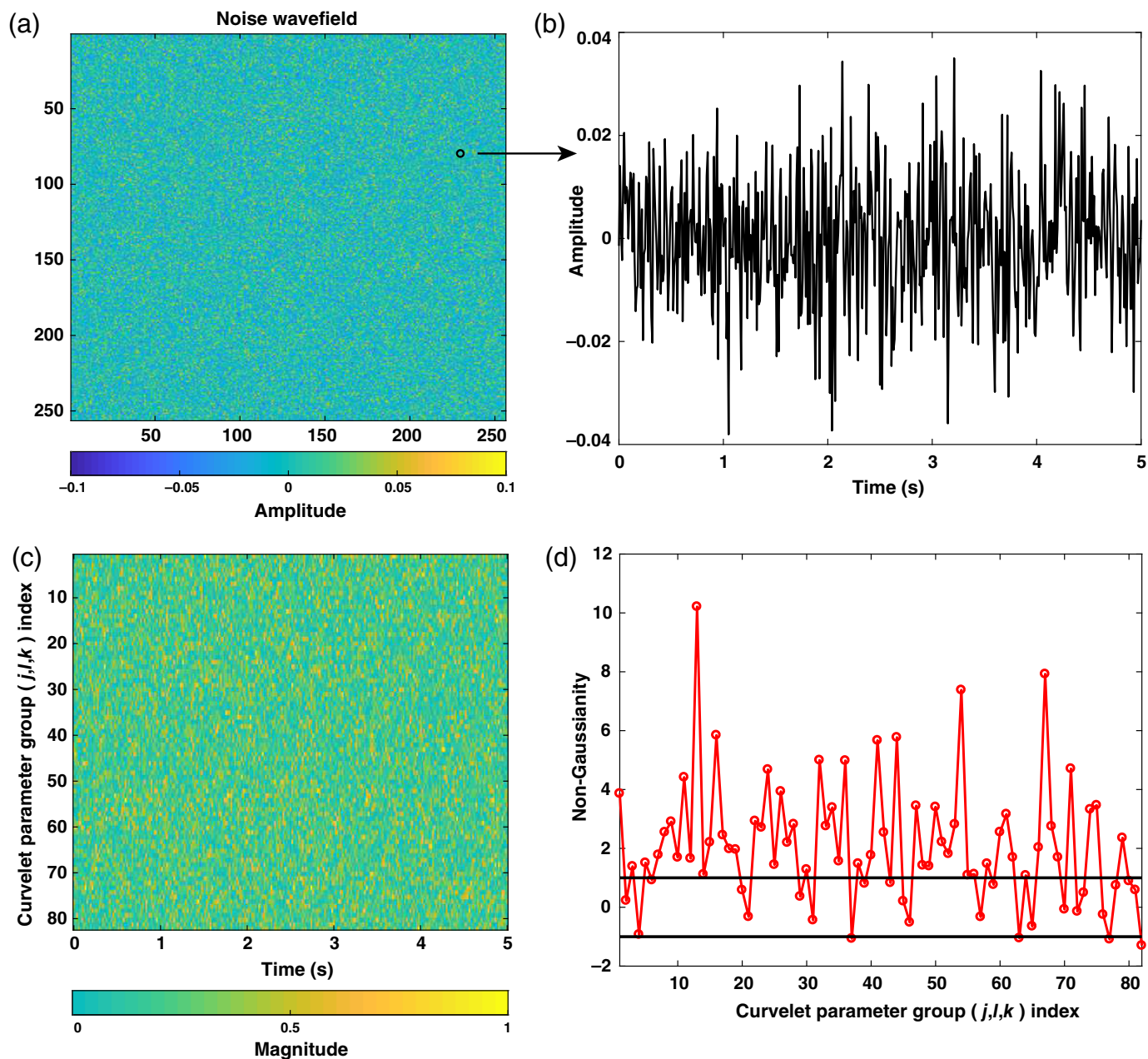
Figure 2. The scheme for developing an in situ scalogram from a 3D curvelet matrix. (a) displays one wavefield snapshot for a synthetic spherical wave. The station chosen for obtaining the scalogram is denoted by a red star. (b) The corresponding curvelet coefficient at each scale j and direction l . The curvelet coefficients assigned to the station is represented by a red square at each (j, l) group. (c) The constructed scalogram by collecting all the curvelet coefficients in time. The color version of this figure is available only in the electronic edition.

whether the magnitude of noise coefficients can be addressed by a Gaussian solution, we compute their kurtosis (the fourth standardized moment), which was introduced in statistics to determine if the input data are Gaussian (Bickel and Doksum, 2015). Regarding the kurtosis of a normal distribution with a value of 3, the excess kurtosis (kurt) for an N -sample data series: $z_n = \{z_1, z_2, \dots, z_N\}$ with a mean μ_z and standard deviation σ_z is defined as follows:

$$\text{kurt} = \frac{\sum_{n=1}^N (z_n - \mu_z)^4}{N} - 3. \quad (8)$$

Then a kurtosis estimator E_{kurt} can be applied to calculate the value of “non-Gaussianity” based on the kurt measurement:

$$E_{\text{kurt}} = \frac{\text{kurt} \sqrt{1-a}}{\sqrt{24/N}}, \quad (9)$$



in which a stands for the level of confidence, usually taking the value of 90% (Ravier and Amblard, 2001). Normally, the input dataset can be classified as Gaussian if the magnitude of E_{kurt} is < 1 (i.e., $|E_{\text{kurt}}| \leq 1$) and non-Gaussian otherwise (for $|E_{\text{kurt}}| > 1$).

We construct a 256×256 pixels synthetic noise field to test the applicability of Gaussian noise assumption (Fig. 3a). The white Gaussian noise at each station, which has a 50 samples per second sampling rate and 5 s duration, is modeled using the built-in add white Gaussian noise function within MATLAB (www.mathworks.com/products/matlab, last accessed November 2023) (Fig. 3b) and is added to each sampling point of the synthetic spherical wave (Fig. 2a) with an SNR of -15 dB. The developed scalogram at a specified station within the noise window displays a random distribution of noise coefficients over lag time

Figure 3. (a) Snapshot in time $t = 1.0$ s for a 256×256 pixels synthetic Gaussian noise field. (b) The synthetic time series of noise at a certain station (denoted by a black circle in panel a) by assuming a white Gaussian distribution. (c) The constructed scalogram at the station showing the distribution of noise coefficient magnitudes in each curvelet parameter group (j, l, k) over time lag. (d) The computed non-Gaussianity of the noise coefficient magnitudes for each (j, l, k) group in panel (c). The non-Gaussianity having values of -1 and 1 are represented by black solid lines. The color version of this figure is available only in the electronic edition.

in different curvelet parameter group (j, l, k) (Fig. 3c). We compute the non-Gaussianity of the magnitude of noise coefficients in all (j, l, k) groups for the synthetic Gaussian noise through the kurtosis test. The result demonstrates that a majority of the non-Gaussianity values are positive and > 1 , indicating non-Gaussian

distributed noise coefficient magnitudes. In addition, a positive kurtosis represents a heavy tail in the distribution (DeCarlo, 1997), implying that the Gaussian noise shows a poor concentration in the curvelet domain and may have a large number of outliers if using the universal threshold in equation (7). Therefore, a more robust criterion than the Gaussian solution should be sought for a better determination of the noise threshold.

Recently, Langston and Mousavi (2019) have proposed the ECDF method to analyze the noise power. The ECDF is calculated by sorting the N -sample noise coefficient magnitudes in ascending order and the corresponding cumulative distribution function (CDF) counts from 0 to 1 with an increment of $1/N$. Based on the empirical estimation of the noise coefficient sequences at each (j, l, k) group, the threshold function $\beta_{j,l,k}$ is decided by taking the value of where the ECDF is at a user-defined tolerance level. Using this method, we do not need to assume a particular noise distribution, such as a Gaussian noise, but let the data choose the correct path. Herein, we estimate the ECDF of noise coefficient at each (j, l, k) group and then determine the threshold by calculating the 99% confidence value for the distribution. In other words, the threshold $\beta_{j,l,k}$ can be properly obtained when the inverse ECDF has a probability of 0.99 (Langston and Mousavi, 2019),

$$\beta_{j,l,k} = \text{ECDF}^{-1}(P_{j,l,k} = 0.99), \quad (10)$$

in which ECDF^{-1} is the inverse CDF, or quantile function, of curvelet coefficients and $P_{j,l,k}$ denotes the probability.

We further apply the ECDF method on a dataset from a dense nodal array deployed in Ohio during August 2013. Figure 4a displays a 60 s raw seismogram from a local event at one station and the corresponding scalogram showing the curvelet coefficient magnitudes. The values in curvelet parameter groups (j, l, k) having a same scale j but different l and k are normalized by the maximum in this scale j . Obviously, curvelet coefficients of signals have larger magnitudes than those in the noise window. Even within a same scale j , the signal-related coefficients in some (l, k) groups are greater than others because the orientations in these groups overlap much with the wave propagation direction. The noise coefficient magnitudes within the first 30-s pre-event window show distinct non-Gaussian statistics through the kurtosis test (Fig. 4b). A comparison of thresholds determined by the ECDF method with universal thresholds assuming Gaussian statistics is displayed in Figure 4c. The magnitude of noise coefficients in coarser (lower) scales overwhelm those in finer scales because a curvelet at coarser scale occupies a larger wavelength in space. However, there are major differences between the thresholds given from these two approaches. The Gaussian criterion will result in a considerable underestimation of threshold because most of the noise coefficient magnitudes have large positive values of non-Gaussianity. Conversely, the thresholds obtained from an inverse ECDF are generally greater than

those from the Gaussian criterion, which are more evident at coarser scales (Fig. 4c), suggesting that the ECDF technique outperforms the universal threshold and yields a better estimation of thresholds. Figure 4d shows the computed ECDF curve from the first 30 s noise window and the resulting threshold at one curvelet parameter group having a non-Gaussianity of 12.57. The threshold in coefficient magnitude is chosen corresponding to where the inverse ECDF has a probability of 0.99.

After the threshold $\beta_{j,l,k}$ has been estimated individually at each (j, l, k) group via the ECDF method, a hard and/or soft thresholding procedure can be performed to denoise the raw data using equations (4) and (5). The remaining curvelet coefficients, $\tilde{C}_{j,l,k}^{D^n}$, after the thresholding are attributed to the seismic signal \tilde{S} , which can be retrieved by applying an inverse curvelet transform for a summarization of the dot product of thresholded coefficients and the curvelet $\phi_{j,i,k}$:

$$\tilde{S}(\bar{x}, t_n) = \sum_{j,l,k} \tilde{C}_{j,l,k}^{D^n} \times \phi_{j,i,k}. \quad (11)$$

On the other hand, by extracting the signal coefficients $\tilde{C}_{j,l,k}^{D^n}$ and keeping only the noise coefficients, the proposed denoising technique can be reversed for data designating. The partitioned signal and noise can be used for a detailed analysis of the structure and source physics (e.g., Yang, Liu, and Langston, 2020; Zhang and Langston, 2022), although it is beyond the scope of this study.

SYNTHETIC TEST

We compute synthetic seismograms using a frequency–wave-number integration method (Zhu and Rivera, 2002) at a dense square array, which is composed of 32×32 stations with an interstation distance of 200 m. A double couple source is placed at a depth of 10 and 80 km away from the array center with an azimuth of 90° . A 1D community velocity model (Lin *et al.*, 2007) combined with attenuation models (Q_p and Q_s) in southern California (Hauksson and Shearer, 2006) is adopted here (Table 1). The synthetic seismograms have a sampling rate of 50 samples per second. The real seismic noise is taken from a dense array deployed in Long Beach, California, consisting of >2000 stations with an average spacing of 120 m (Lin *et al.*, 2013) and added to the synthetics with an SNR of 3, which was calculated by a ratio of the mean amplitude within the signal time window to that within the noise window.

We process the synthetic waveform with the above procedure. We first measure the noise level in an 8-s presignal window after the curvelet transform followed by a determination of noise threshold in each curvelet parameter group though the ECDF method. Then we apply hard and soft thresholding to remove the noise coefficients and recover the denoised signals via the inverse curvelet transform. The results show that most of the background noise is removed successfully by nonlinear thresholding methods. The denoised signals are mainly compatible to the original synthetics, not only in phase arrival but also

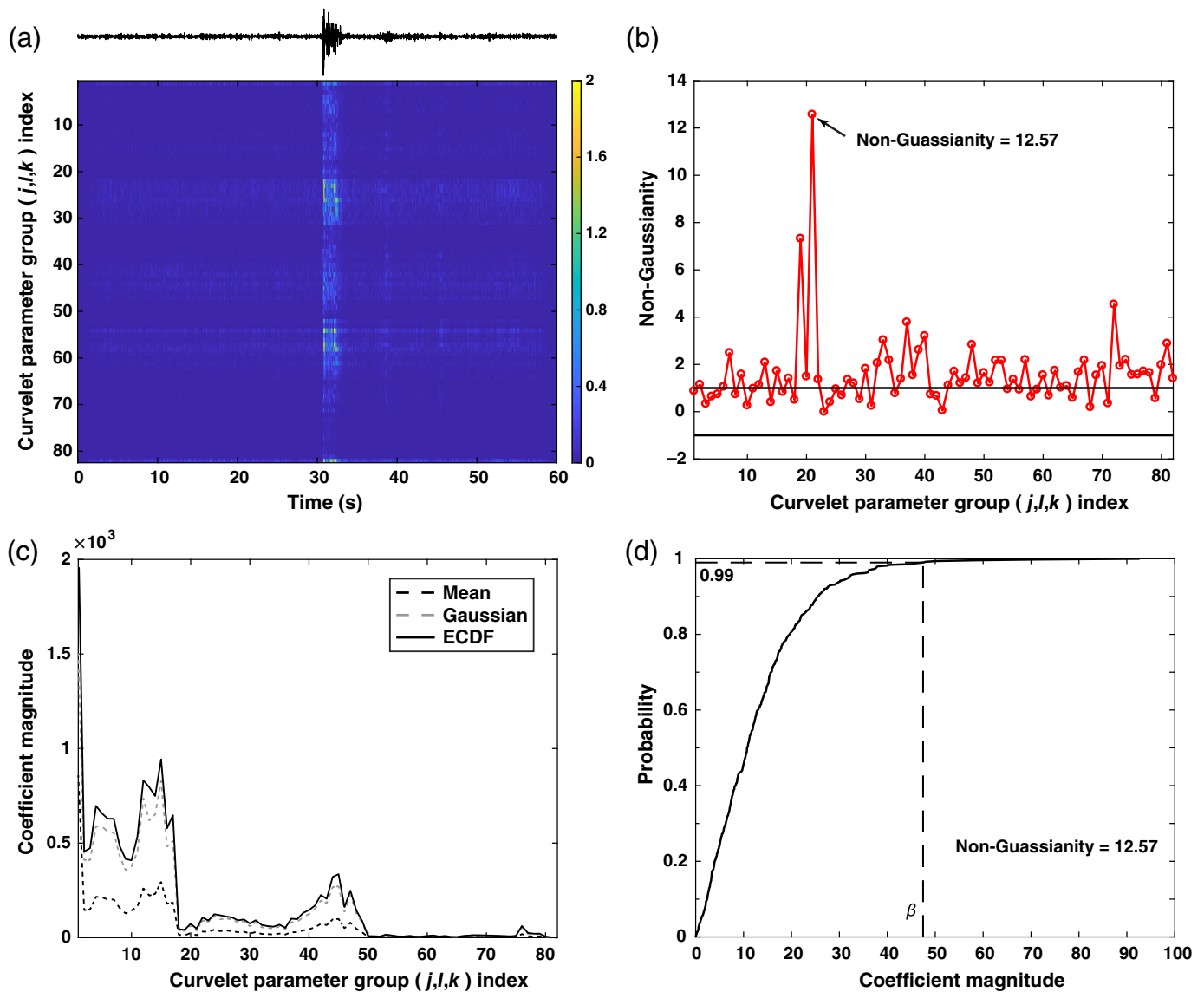
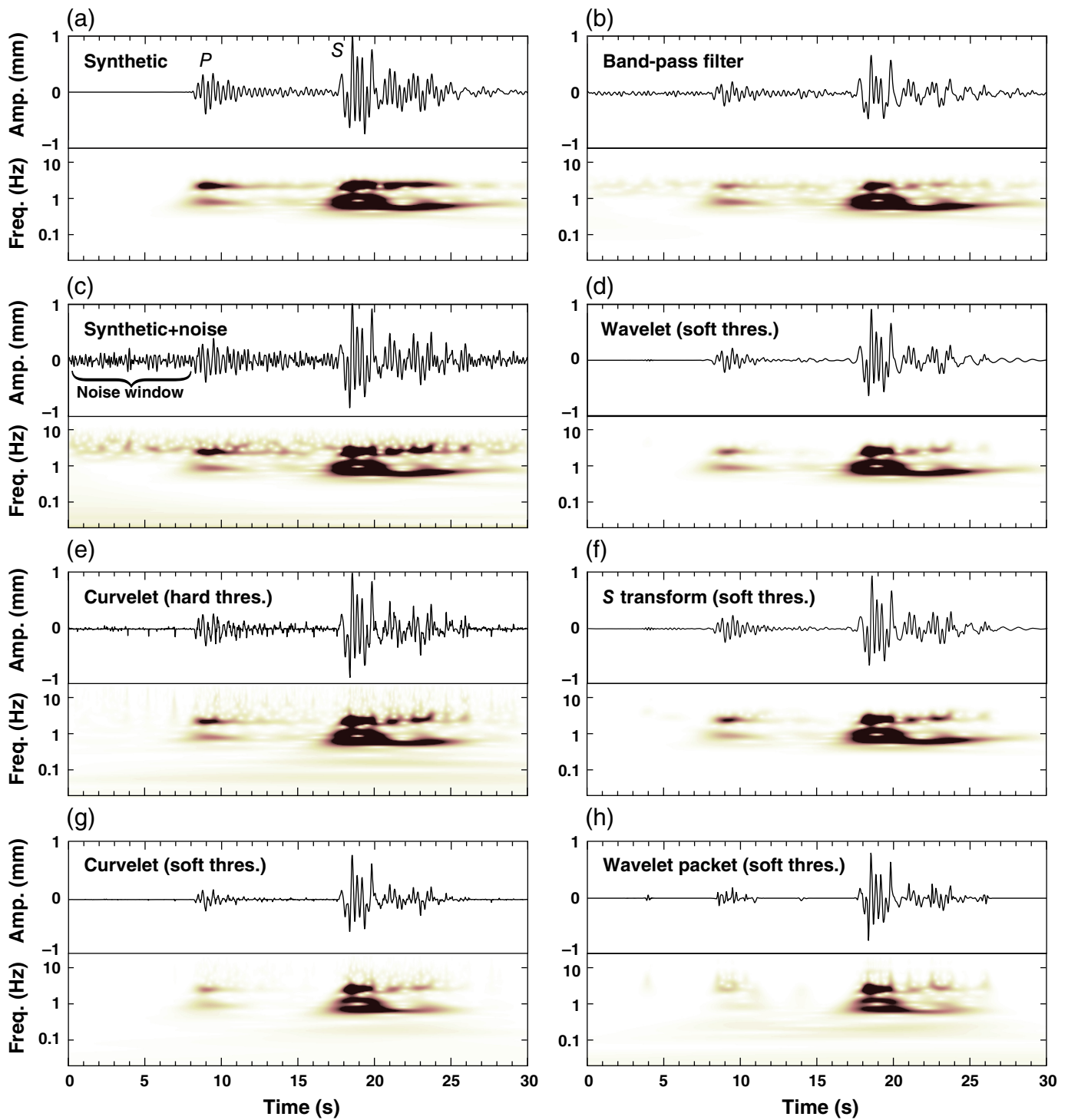


Figure 4. (a) The raw seismogram for a local event and corresponding scalogram of the curvelet coefficient magnitudes over a 60 s duration time at one station from a dense nodal array deployed in Ohio during August 2013. A coarser curvelet scale has a smaller parameter group index. (b) The statistics of the absolute value of noise coefficients within the first 30 s time window. The non-Gaussianity having values of -1 and 1 are represented by black solid lines. A black arrow points out a curvelet parameter group having a

non-Gaussianity of 12.57. (c) Comparison of the mean magnitude of noise coefficients in different (j, l, k) groups with two different thresholding functions calculated by the empirical cumulative distribution function (ECDF) method and Gaussian criterion. (d) The computed ECDF curve for the curvelet parameter group having a non-Gaussianity of 12.57. The threshold β is determined with a probability of 0.99. The color version of this figure is available only in the electronic edition.

TABLE 1
1D Background Velocity, Density, and Attenuation Model for Synthetic Seismogram Simulation

Depth (km)	V_S (km/s)	V_P (km/s)	Density (g/cm^3)	Q_S	Q_P
0.5	0.80	2.0	1.55	70	150
1.5	2.88	5.0	2.65	150	300
5.5	3.17	5.5	2.73	300	500
9.5	3.63	6.3	2.85	600	1200
15.5	3.70	6.4	2.88	400	800
33	3.93	6.8	2.94	500	1000
50	4.50	7.8	3.10	500	1000



in waveform shape, validating the effectiveness of our curvelet method (Fig. 5a,c,e,g). Furthermore, it is evident that soft thresholding surpasses hard thresholding in enhancing SNR (Fig. 5e,g). The characteristics of main phases, for example, *P* and *S* waves, are mostly preserved after denoising. However, the amplitudes of some phases are unexpectedly reduced, especially for *P*- and *S*-coda waves, because their amplitudes are almost at the same level as the background noise.

We also compare the performance of our curvelet method with digital filtering and other widely used approaches such

Figure 5. Seismograms recorded at one station of the virtual dense array for (a) synthetic, (c) synthetic added with Long Beach array noise, signal denoised by (e) hard thresholding, and (g) soft thresholding using the curvelet-based ECDF method compared with the denoised signal using a (b) Butterworth band-pass (0.2–3 Hz) filter, (d) wavelet, the *S* transform, and (h) wavelet packet technique. The corresponding continuous wavelet transform (CWT) scalogram representing the frequency content distributions over time is shown below each subfigure. The wavelet, *S* transform, and wavelet packet technique are all implemented with the level-dependent universal threshold. The color version of this figure is available only in the electronic edition.

TABLE 2

Quantitative Comparison among the Synthetic and the Signal Denoised by Several Methods

Methodology	SNR	<i>P</i> Wave Arrival Delay (s)	Spectral Loss (%)	Correlation Coefficient
Synthetics added with noise	3	0.04	−43.3	0.892
Curvelet (ECDF)	145	0.00	8.0	0.922
Butterworth band-pass filter	7	0.02	21.7	0.900
Wavelet (universal threshold)	153	0.01	15.3	0.915
<i>S</i> transform (universal threshold)	111	0.01	15.6	0.920
Wavelet packet (universal threshold)	79	0.03	10.6	0.895

ECDF, empirical cumulative distribution function; SNR, signal-to-noise ratio.

as wavelets, the *S* transform, and the wavelet packets (Fig. 5b, d,f,h). A zero-phase Butterworth filter was used to filter the seismogram between 0.2 and 3 Hz, which is the most energetic frequency band for the synthetic signal. The wavelet, *S* transform, and wavelet packet methods are all implemented with the level-dependent universal threshold and applied to denoise the data by soft thresholding. To get a better understanding of the strength and weakness of all of the methods, a detailed quantitative evaluation of the improvement in SNR, *P*-wave arrival difference, spectral losses, and waveform similarity is provided in Table 2. Herein, the spectral loss is calculated by measuring the overall change in Fourier spectrum after denoising and that of the noise-free synthetic signal over a frequency band of 0.02–25 Hz, which mostly reflects the difference in the frequency content. A negative spectral loss or a valid spectral abundance is attained because the introduced noise generally has a broader frequency coverage. The quantitative results clearly demonstrate that our curvelet method achieves the fewest spectral losses, which is anticipated because the curvelet transform and subsequent thresholding are conducted in the spatial domain rather than the time–frequency domain. Moreover, the curvelet method achieves the highest correlation coefficient and smallest time delay of *P*-wave arrival, further verifying the efficiency of our curvelet method. The application of band-pass filtering does not effectively remove the noise, but other methodologies can successfully improve the SNR. The highest SNR of ~153 is obtained by wavelets, slightly higher than the results using curvelets (~145).

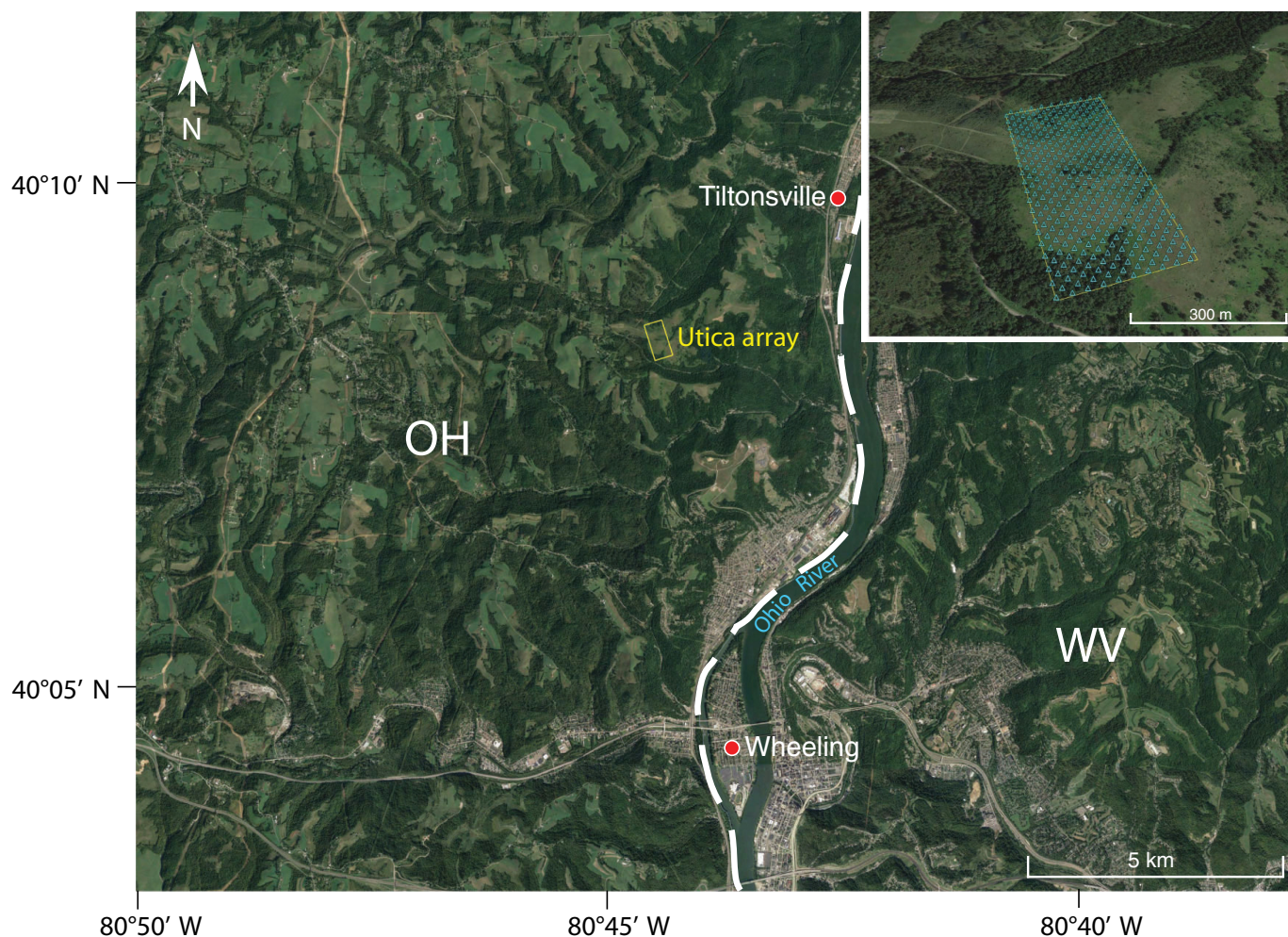
To investigate the effect of noise window length during the thresholding, we chose different time durations to estimate the noise thresholds (Table 3). Obviously, noise can be compressed much more with a longer length because the thresholds determined by the ECDF method are more precise with larger amounts of noise samples. For example, compared with a 2 s noise window (or 100 noise samples), using a 6 s noise window (or 300 noise samples) drastically improves the SNR from ~47 to 140 by soft thresholding. On the other hand, a limited improvement of SNR ~147 is attained with an 8 s noise window. The results suggest taking a noise window with an approximating noise sample of ~300–500 is good enough for seismic denoising using stationary noise data.

APPLICATIONS ON DENSE ARRAY DATA

As part of the Utica 3D field experiment by Global Geophysical Services, a dense array composed of 400 AutoSeis high frequency seismometers (4–84 Hz bandwidth) with an average spacing, Δd , of 30 m has been deployed in Belmont County, Ohio, for one month since 23 August 2013 (Fig. 6). The passive data records include local high-frequency quarry blasts and global earthquakes.

The raw datasets are stored in SEGY format every 60 s. We inspect all the waveforms recorded by the array and removed null traces. Because the seismic signals mostly occupy the frequency contents of 0.1–20 Hz, we decimate the demeaned and detrended seismograms to a sample rate of 50 Hz to improve the computation efficiency. Here, we chose two example recordings to demonstrate noise reduction by curvelets. To avoid the irregular spacing of the original dataset, a second-order polynomial interpolation is used to create a smoothly varying spatial mesh before transferring the wavefield to curvelet domain (Fig. 7a,b). To minimize the misfit between the interpolated wavefield and the raw data, we calculate the misfit before and after remeshing by summing the distance between stations and the nearest interpolated point. After testing, 256 × 256 grid points with an average grid spacing of 2 m are optimal to obtain an equal-spaced wavefield with a small total misfit of ~9 m (or $0.3 \times \Delta d$) (Fig. 7c,d). As implemented, the curvelet transform expands a 256 × 256 spatial wavefield to a curvelet coefficient matrix with scales ranging from 1 to 5 (Candes *et al.*, 2006). In our cases, the spatial frequency or wavelength of scale 1 is $> \sim 60$ m. Scales 2, 3, 4 give wavelengths of ~60–30 m, ~30–15 m, and ~15–8 m, respectively. The finest scale of 5 has a wavelength $< \sim 8$ m, smaller than the misfit of ~9 m.

The first example contains wavefield from a high-frequency 2 lb dynamite shot event (labeled as event 1) with high noise level. A presignal window of 13 s is used to calculate the noise thresholds. No filter is applied to the data before performing the curvelet method. As shown in two individual time snapshots (Fig. 8), the noise fields are effectively removed by the curvelet method (Fig. 8c,d), particularly evident for the pre-event one (Fig. 8b). Moreover, the signal propagation pattern is preserved without major distortion by thresholding. Signals arising at



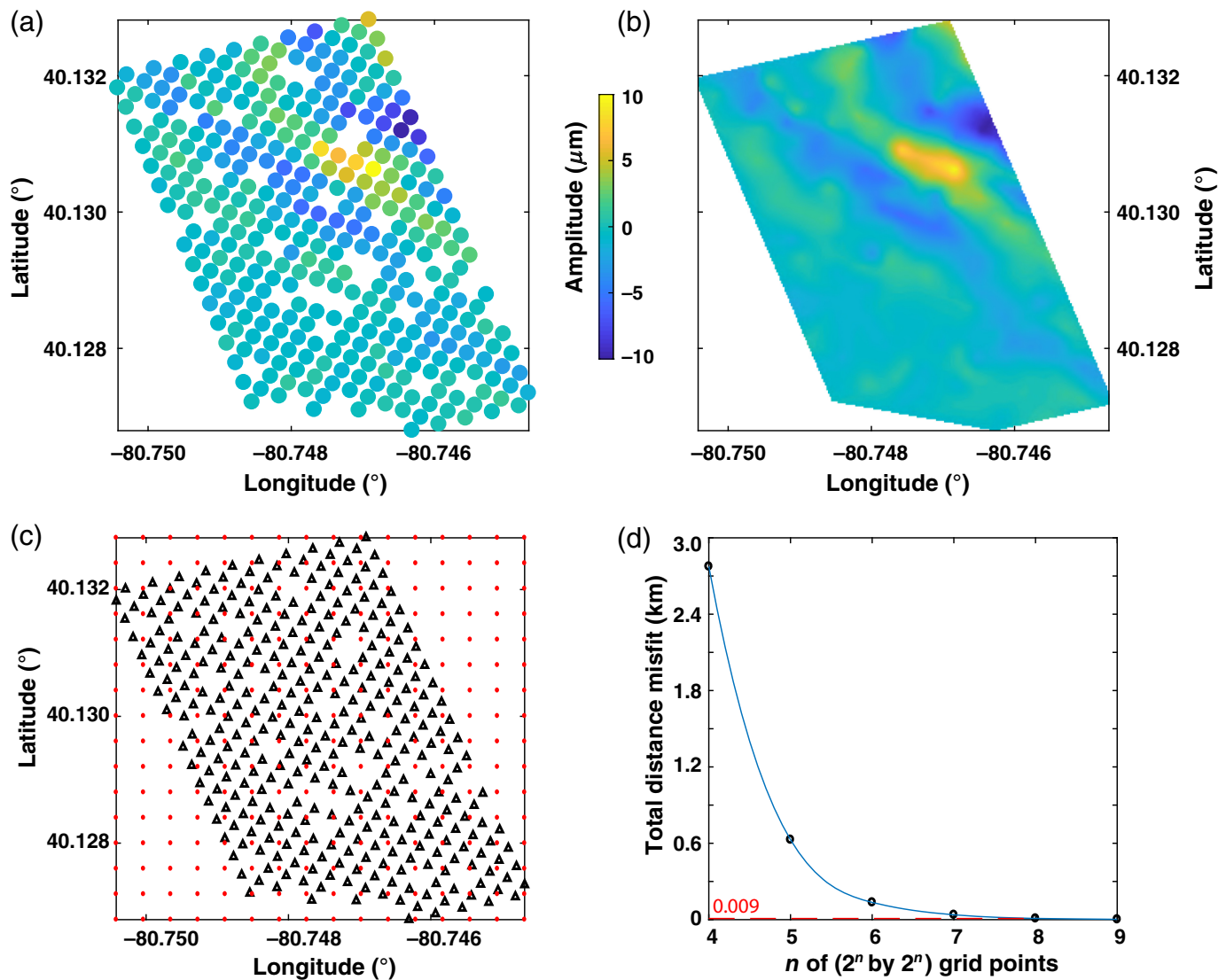
around 14.1 s are identified as high-frequency body waves with a group velocity of ~ 4.5 km/s from the shot located to the south-southeast. By inspecting the waveform at one station, we find that most of the background noise is successfully removed (Fig. 9). We also note some small amplitudes within the whole duration for hard thresholding, probably caused by an incomplete removal of noise coefficients. Conversely, SNR has been much improved through soft thresholding, increasing from 2.5 to 131.6.

Another example is teleseismic P waves from an M_w 7.0 earthquake that occurred in the Aleutian Islands (labeled as event 2). A 20-s noise window is chosen for determining the noise power. Results from hard and soft thresholding show that background noise is significantly reduced (Fig. 10a–c). Soft thresholding outperforms hard thresholding with a higher SNR after denoising, increasing from 5.1 to 126.3. Not only the earthquake signal is recovered robustly from the noisy raw data, but the curvelet method also yields an accurate estimate of the noise by designating (Fig. 10d). Therefore, application of soft thresholding for dense array data is an effective way to separate wavefield into signals and noises.

Figure 6. Image from Google Earth showing the location and configuration (inset) of Utica array deployed in Belmont County, Ohio. The Ohio–West Virginia state boundary is denoted by a white dashed line. The color version of this figure is available only in the electronic edition.

DISCUSSION

The curvelet-based denoising method has yielded success in improving SNR and preserving signal waveforms for synthetic and observational data. Background noise can be removed successfully by choosing a long enough pre-event window to estimate the noise level. Compared with the traditional Fourier-based and wavelet denoising procedures, the curvelet technique provides an effective way to handle a large 2D array dataset and process all the waveform data per snapshot. After mapping the wavefield amplitudes into the curvelet domain, the noise coefficients at finer scales (or larger spatial frequency) reflect contributions of local or regional noise sources. Averaging over all array channels in such scales tends to remove these coefficients because they only exist at part of stations. This characteristic is an improvement over wavelet techniques because noise on individual seismograms will go into



thresholding in the application of wavelets without considering adjacent stations. Figure 11 demonstrates this with a comparison of the soft-thresholded signals of event 2 using curvelets, wavelets, the S transform, and wavelet packets. All techniques result in significant improvement in SNR. Among these, the signal recovered by curvelets has the highest SNR of 126 and shows a broader frequency range but a slightly sharper waveform change compared with that from the wavelet and S transform analyses. The wavelet packet method also shows fewer frequency losses but has a less improved SNR of 81. Although the application of curvelet method implemented

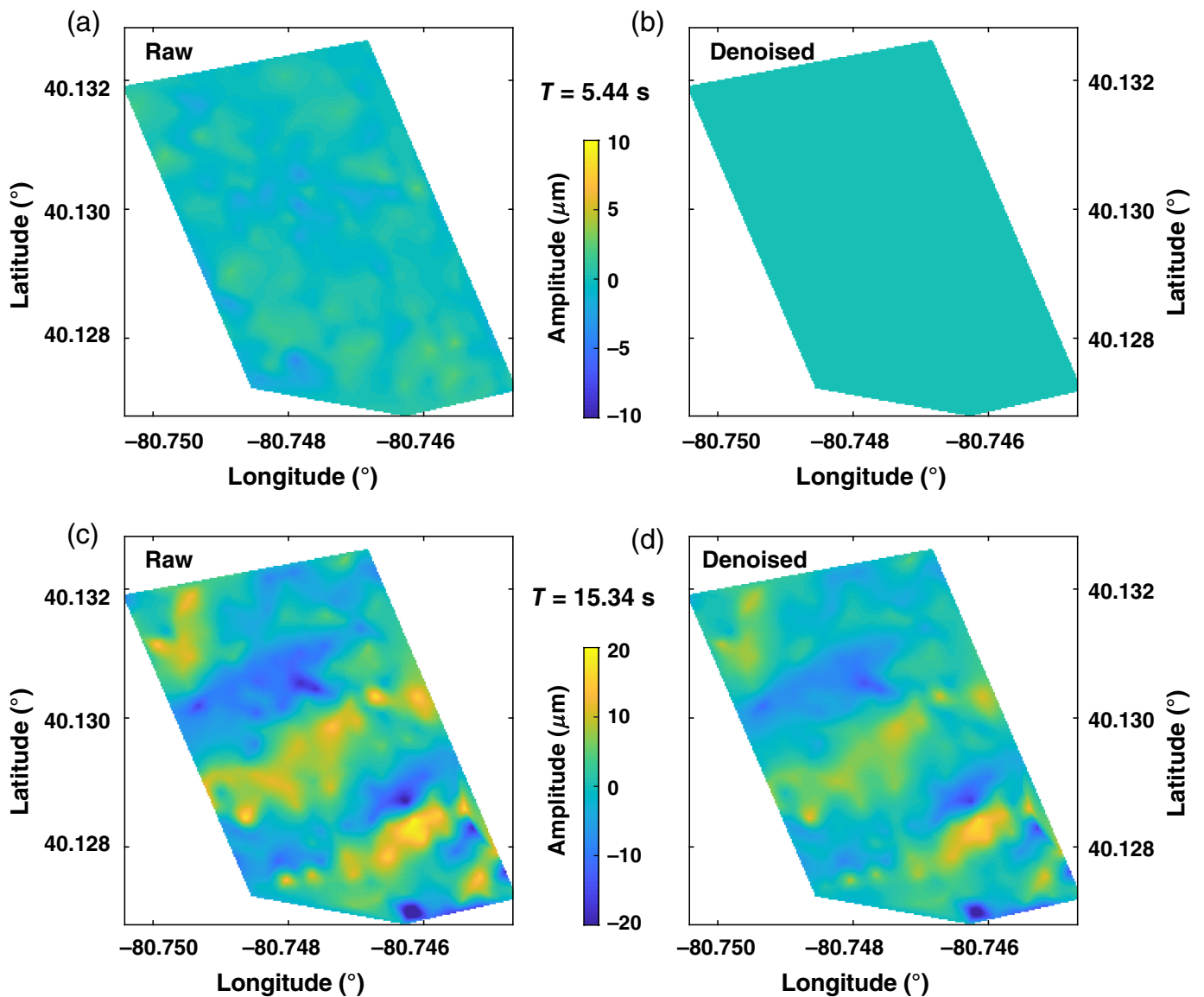
Figure 7. (a) Raw wavefield observed by the Utica array at time 5 September 2013 15:08:51 (UTC). The dot represents the waveform amplitude recorded at each station. (b) Interpolated wavefield with 256×256 grid points. (c) The location of 16×16 interpolated grid points (red dots) and original stations (black triangles). (d) The total distance misfit between the station and the nearest interpolated point with 2^n ($n = 4, 5, 6, 7, 8, 9$) grid points at a side (black dots). The interpolated matrix of 256×256 grid points gives an overall relative distance misfit of ~ 9 m. The color version of this figure is available only in the electronic edition.

TABLE 3

Improved Signal-to-Noise Ratio (SNR) by Soft Thresholding in the Synthetic Test Using a Noise Window with Different Time Durations

Length of Noise Window (s)	2	3	4	5	6	7	8
Improved SNR with uncertainty	46.8 ± 7.0	59.1 ± 10.1	74.8 ± 12.7	125.7 ± 11.5	140.6 ± 13.4	145.1 ± 9.2	147.3 ± 7.9

The uncertainty represents a confidence level of 99.7%.



with the nonlinear thresholding on both synthetic and the Utica array data has shown encouraging results, other user-customized threshold methods (e.g., Parolai, 2009) have been shown effective to improve the SNR of array data. The efficiency of different denoising thresholds should be more comprehensively investigated in future studies.

On the other hand, we also notice some limitations of our curvelet technique. One drawback is that curvelet lacks a temporal continuity because it is manipulated for different snapshots, and therefore the 2D spatial wavefield at each time point is treated separately from the others. There is no constraint to ensure smoothness of the wavefield over the lag time. A combination of wavelets in time and curvelets in space could be promising to address this problem (Zhan *et al.*, 2018). On the other hand, the denoising resolution of curvelets is limited by the spatial spacing of the array. For a dense array with an irregular spacing, directly applying the curvelet transform to the nonequispaced wavefield could lead to biased results. To

Figure 8. Display of (a,c) raw wavefield and (b,d) denoised wavefield at two different time snapshots for a 2 lb shot event (labeled as event 1). The original time is 4 September 2013 14:41:00 (UTC). The upper two maps (a) and (b) are for time $t = 5.44$ s before the body wave arrives and 15.34 s after the signal arrival for the bottom maps (c) and (d). Notes that the color bars have different ranges for upper and lower maps. The color version of this figure is available only in the electronic edition.

overcome this, we applied a second-order polynomial algorithm to interpolate the original wavefield to a regular grid network prior to the curvelet transform because the seismic wavefronts in 2D space is generally affiliated with an ℓ_2 minimization problem (Zhang and Langston, 2020). This interpolation processing works well for the ultradense Utica array considering that the relative distance misfit (~ 9 m) is much smaller than the wavelength of body waves. However, the second-order polynomial interpolation may underfit for the observations of complicated wavefields, especially for a sparse array. A nonequispaced fast

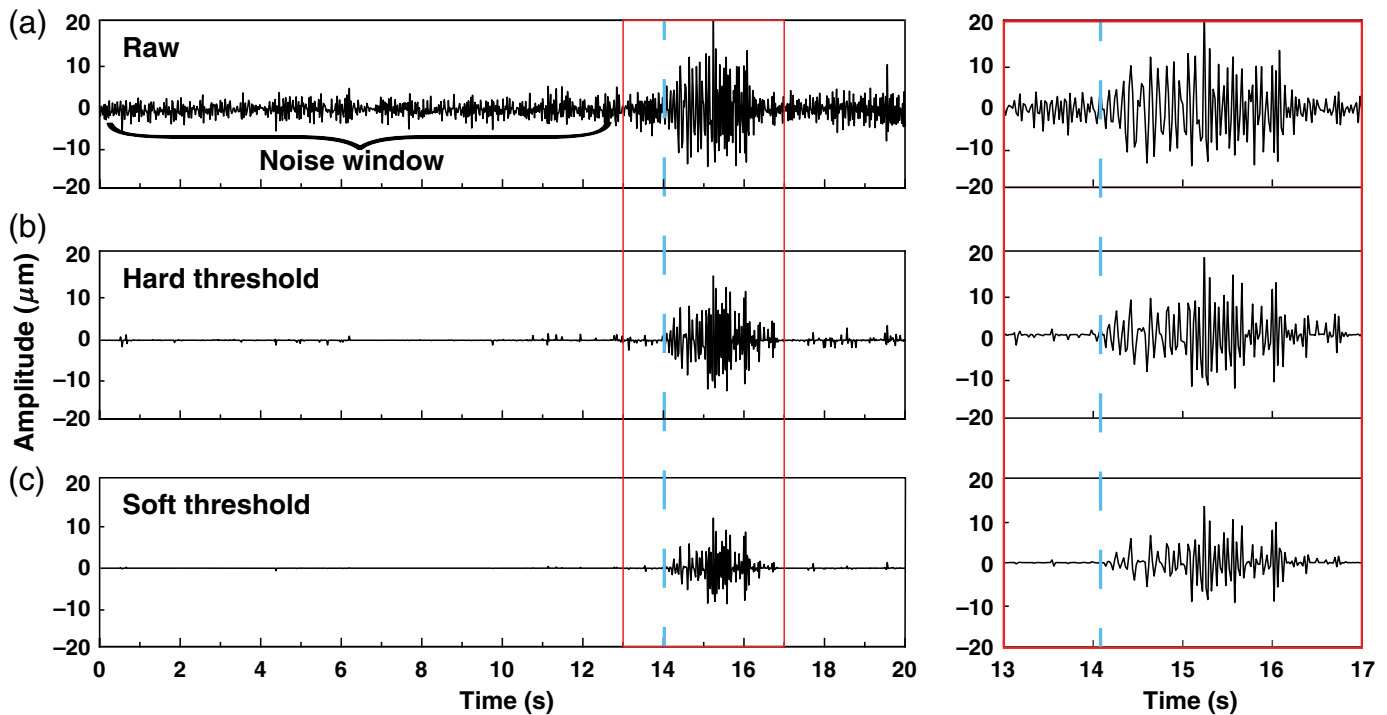


Figure 9. Display of (a) raw seismogram and denoised seismograms by (b) hard and (c) soft thresholding using the ECDF method at one station from the Utica array. The original time is 4 September 2013 14:41:00 (UTC). The red windows outline the body waves of a 2 lb shot (event 1) within 13–

17 s, the details of which are shown in the following magnified plots. The blue dashed lines indicate the first arrival time of body waves around 14.1 s. A 13 s noise window before the event is used for the threshold estimation. The color version of this figure is available only in the electronic edition.

discrete curvelet transform method (Hennenfent *et al.*, 2010) may provide an alternative to resolve the regularization of irregularly sampled data.

As in any denoising scheme, the performance of noise reduction depends on the noise level. Noises can be separated from signals for regions with high SNR. However, coda portions of waveforms can have similar properties as the background noise and are preferentially reduced. Signals close to the noise threshold can also be severely reduced. With wavelet methods, the success of thresholding demands data with high SNR in some portion of the transform space. The strength of using curvelets is that continuous wave-like features will be preserved at the expense of more random spatial fluctuations in ground motions. Moreover, although the curvelet method proposed in this study is initially designed to denoise data of 2D arrays, it is also applicable to 1D arrays by modifying the transformation to convert time-domain waveform data (distance–time) into the curvelet domain instead of using 2D spatial wavefield data, which has been basically described by Herrmann *et al.* (2007).

CONCLUSION

We propose a curvelet-based denoising method to remove the background noise recorded on dense 2D seismic arrays. The

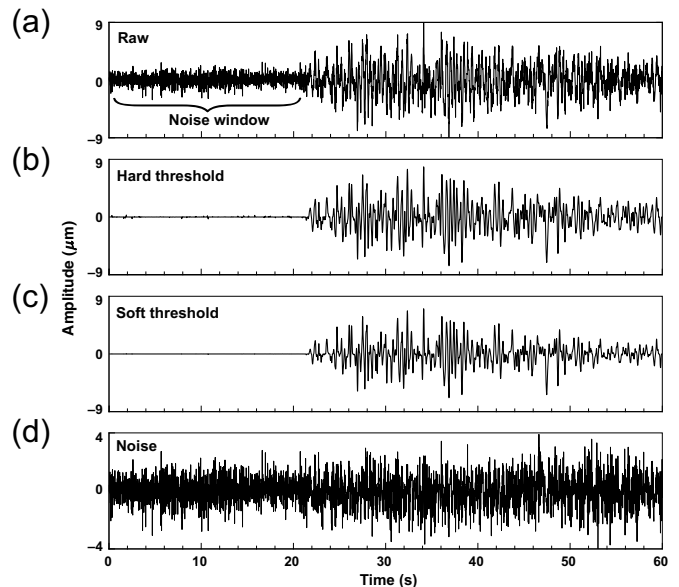
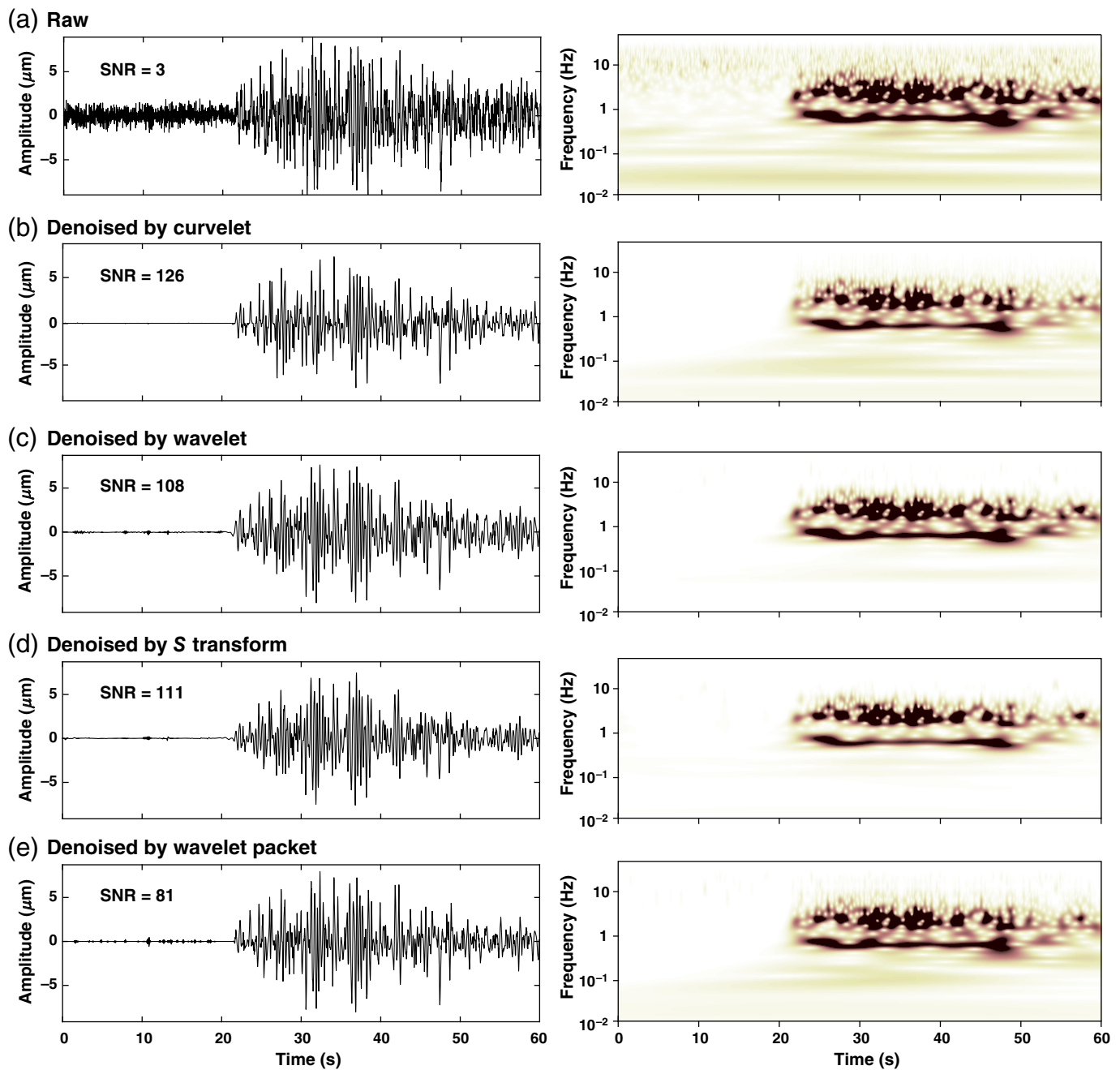


Figure 10. Time-series plot of (a) raw seismogram, (b) hard threshold denoised signal, (c) soft threshold denoised signal and (d) noise for the 30 August 2013 M_w 7.0 Aleutian earthquake (labeled as event 2). The original time is 30 August 2013 16:35:00 (UTC). A 20 s noise window before the P arrival is used for the threshold estimation. Note that there is a smaller amplitude range in the noise plot.



noise fields within a pre-event window are used to estimate the thresholds via a detailed characterization of the noise power in the curvelet domain. A synthetic test and application on data from the Utica array illustrate the effectiveness of nonlinear thresholding by the ECDF method. For nearly Gaussian noise, a more ideal denoising result is achieved with curvelets through the ECDF approach compared with the conventional curvelet techniques. This approach provides a new option besides the traditional Fourier and wavelet denoising methods to recover signals for dense arrays. The partitioned noise can be used for seismic interferometry studies, and the denoised seismograms will lead to an advanced earth structure imaging or source physics characterization.

Figure 11. Time-series plot and corresponding CWT scalograms of event 2 (a) raw seismogram and soft-thresholded signals based on (b) curvelets, (c) wavelets, (d) the S transform, and (e) wavelet packet method. The CWT scalogram represents the energy distribution over frequency and time. The color version of this figure is available only in the electronic edition.

DATA RESOURCES

The Long Beach array data used in this study is the property of Nodal Seismic and Signal Hill Petroleum Inc., and permission from them is required to access it. The codes for fast digital curvelet transform are described by [Candes *et al.* \(2006\)](#). Matlab software for continuous wavelet transform (CWT)

processing is introduced by Langston and Mousavi (2019) and available from the coauthor's website at <http://www.ceri.memphis.edu/people/clangstn> (last accessed July 2022). The frequency–wavenumber (f - k) seismic package used for computing synthetic seismograms is provided by Lupei Zhu (Zhu and Rivera, 2002). Google Earth, published by Google Inc. (<https://www.google.com/earth>; last accessed September 2023) is used in this article and is gratefully acknowledged. Although raw data from the Utica array are embargoed by Global Geophysical Services, the supplemental material includes the short time section of processed data for the two event recordings that we analyzed.

DECLARATION OF COMPETING INTERESTS

The authors acknowledge that there are no conflicts of interest recorded.

ACKNOWLEDGMENTS

This research was supported by the National Natural Science Foundation of China (Grant Number U2139203), the Hong Kong Special Administrative Region (HKSAR) Research Grant Council General Research Fund (GRF) Grant Numbers 14306122 and 14303721, the Chinese University of Hong Kong (CUHK) Direct Grant from Faculty of Science, and State Key Lab of Earthquake Dynamics (Grant Number LED2021B03). The authors would like to thank Associate Editor Stefano Parolai, as well as two anonymous reviewers for their constructive and insightful comments.

REFERENCES

Basak, R. L., K. S. Rana, A. K. Rao, A. Gangaiah, and C. R. Chandrasekaran (2012). Removal of noises using Tau-P transformation—an indigenous tool for noise attenuation in shallow seismic data, *9th Biennial International Conference & Exposition on Petroleum Geophysics*, Hyderabad, 16–18 February 2012, Vol. 6, 2012 pp.

Behm, M., G. M. Leahy, and R. Snieder (2014). Retrieval of local surface wave velocities from traffic noise—an example from the La Barge basin (Wyoming), *Geophys. Prospect.* **62**, no. 2, 223–243.

Bendat, J. S., and A. G. Piersol (2011). *Random Data: Analysis and Measurement Procedures*, Vol. 729, John Wiley & Sons, New Jersey.

Ben-Zion, Y., F. L. Vernon, Y. Ozakin, D. Zigone, Z. E. Ross, H. Meng, M. White, J. Reyes, D. Hollis, and M. Barklage (2015). Basic data features and results from a spatially dense seismic array on the San Jacinto fault zone, *Geophys. J. Int.* **202**, no. 1, 370–380.

Bickel, P. J., and K. A. Doksum (2015). *Mathematical Statistics: Basic Ideas and Selected Topics, Volumes I-II Package*, CRC Press, Florida.

Candes, E. J., and L. Demanet (2003). Curvelets and Fourier integral operators, *C.R. Math.* **336**, no. 5, 395–398.

Candes, E. J., and L. Demanet (2005). The curvelet representation of wave propagators is optimally sparse, *Commun. Pure Appl. Math.* **58**, no. 11, 1472–1528.

Candes, E., L. Demanet, D. Donoho, and L. Ying (2006). Fast discrete curvelet transforms, *Multiscale Model. Sim.* **5**, no. 3, 861–899.

Chang, S. G., B. Yu, and M. Vetterli (2000). Adaptive wavelet thresholding for image denoising and compression, *IEEE Trans. Image Process.* **9**, no. 9, 1532–1546.

DeCarlo, L. T. (1997). On the meaning and use of kurtosis, *Psychol. Meth.* **2**, no. 3, 292–307, doi: [10.1037/1082-989X.2.3.292](https://doi.org/10.1037/1082-989X.2.3.292).

Ditommaso, R., M. Mucciarelli, and F. C. Ponzio (2012). Analysis of non-stationary structural systems by using a band-variable filter, *Bull. Earthq. Eng.* **10**, 895–911.

Donoho, D. L., and I. M. Johnstone (1994). Ideal spatial adaptation by wavelet shrinkage, *Biometrika* **81**, no. 3, 425–455.

Donoho, D. L., and I. M. Johnstone (1995). Adapting to unknown smoothness via wavelet shrinkage, *J. Am. Stat. Assoc.* **90**, no. 432, 1200–1224.

Douglas, A. (1997). Bandpass filtering to reduce noise on seismograms: Is there a better way? *Bull. Seismol. Soc. Am.* **87**, no. 3, 770–777.

Gaci, S. (2013). The use of wavelet-based denoising techniques to enhance the first-arrival picking on seismic traces, *IEEE Trans. Geosci. Remote Sens.* **52**, no. 8, 4558–4563.

Galiana-Merino, J. J., J. Rosa-Herranz, J. Giner, S. Molina, and F. Botella (2003). De-noising of short-period seismograms by wavelet packet transform, *Bull. Seismol. Soc. Am.* **93**, no. 6, 2554–2562.

Harmon, N., C. Rychert, and P. Gerstoft (2010). Distribution of noise sources for seismic interferometry, *Geophys. J. Int.* **183**, no. 3, 1470–1484.

Hauksson, E., and P. M. Shearer (2006). Attenuation models (Q_p and Q_s) in three dimensions of the southern California crust: Inferred fluid saturation at seismogenic depths, *J. Geophys. Res.* **111**, no. B5, doi: [10.1029/2005JB003947](https://doi.org/10.1029/2005JB003947).

Hennenfent, G., L. Felon, and F. J. Herrmann (2010). Nonequispaced curvelet transform for seismic data reconstruction: A sparsity-promoting approach, *Geophysics* **75**, no. 6, WB203–WB210.

Herrmann, F. J., and G. Hennenfent (2008). Non-parametric seismic data recovery with curvelet frames, *Geophys. J. Int.* **173**, no. 1, 233–248.

Herrmann, F. J., U. Böniger, and D. J. Verschuur (2007). Non-linear primary-multiple separation with directional curvelet frames, *Geophys. J. Int.* **170**, no. 2, 781–799.

Herrmann, F. J., D. Wang, G. Hennenfent, and P. P. Moghaddam (2008). Curvelet-based seismic data processing: A multiscale and nonlinear approach, *Geophysics* **73**, no. 1, A1–A5.

Huang, B. S. (2001). Evidence for azimuthal and temporal variations of the rupture propagation of the 1999 Chi-Chi, Taiwan earthquake from dense seismic array observations, *Geophys. Res. Lett.* **28**, no. 17, 3377–3380.

Inbal, A., J. P. Ampuero, and R. W. Clayton (2016). Localized seismic deformation in the upper mantle revealed by dense seismic arrays, *Science* **354**, no. 6308, 88–92.

Jiang, X., S. Hu, and H. Yang (2021). Depth extent and V_p/V_s ratio of the Chenghai fault zone, Yunnan, China constrained from dense-array-based teleseismic receiver functions, *J. Geophys. Res.* **126**, no. 8, e2021JB022190, doi: [10.1029/2021JB022190](https://doi.org/10.1029/2021JB022190).

Langston, C. A., and S. M. Mousavi (2019). Separating signal from noise and from other signal using nonlinear thresholding and scale-time windowing of continuous wavelet transforms, *Bull. Seismol. Soc. Am.* **109**, no. 5, 1691–1700.

Li, C., and M. Liang (2012). A generalized synchroqueezing transform for enhancing signal time–frequency representation, *Signal Process.* **92**, no. 9, 2264–2274.

Lin, F. C., D. Li, R. W. Clayton, and D. Hollis (2013). High-resolution 3D shallow crustal structure in Long Beach, California:

- Application of ambient noise tomography on a dense seismic array, *Geophysics* **78**, no. 4, Q45–Q56.
- Lin, G., P. M. Shearer, E. Hauksson, and C. H. Thurber (2007). A three-dimensional crustal seismic velocity model for southern California from a composite event method, *J. Geophys. Res.* **112**, no. B11, doi: [10.1029/2007JB004977](https://doi.org/10.1029/2007JB004977).
- Ma, J., and G. Plonka (2010). The curvelet transform, *IEEE Signal Process Mag.* **27**, no. 2, 118–133.
- Mousavi, S. M., and C. A. Langston (2016). Hybrid seismic denoising using higher-order statistics and improved wavelet block thresholding, *Bull. Seismol. Soc. Am.* **106**, no. 4, 1380–1393.
- Mykkeltveit, S., K. Åstebøl, D. J. Doornbos, and E. S. Husebye (1983). Seismic array configuration optimization, *Bull. Seismol. Soc. Am.* **73**, no. 1, 173–186.
- Naghizadeh, M., and M. D. Sacchi (2010). Beyond alias hierarchical scale curvelet interpolation of regularly and irregularly sampled seismic data, *Geophysics* **75**, no. 6, WB189–WB202.
- Parolai, S. (2009). Denoising of seismograms using the S transform, *Bull. Seismol. Soc. Am.* **99**, no. 1, 226–234.
- Ravier, P., and P. O. Amblard (2001). Wavelet packets and de-noising based on higher-order-statistics for transient detection, *Signal Process.* **81**, no. 9, 1909–1926.
- She, Y., H. Yao, H. Yang, J. Wang, and J. Feng (2022). Constraining the depth extent of low-velocity zone along the Chenghai fault by dense array ambient noise interferometry and horizontal-to-vertical spectral ratio, *Tectonophysics* **827**, 229265, doi: [10.1016/j.tecto.2022.229265](https://doi.org/10.1016/j.tecto.2022.229265).
- Song, J., and H. Yang (2022). Seismic site response inferred from records at a dense linear array across the Chenghai fault zone, Binchuan, Yunnan, *J. Geophys. Res.* **127**, no. 1, e2021JB022710, doi: [10.1029/2021JB022710](https://doi.org/10.1029/2021JB022710).
- Starck, J. L., F. Murtagh, and J. M. Fadili (2010). *Sparse Image and Signal Processing: Wavelets, Curvelets, Morphological Diversity*, Cambridge University Press, Cambridge, United Kingdom.
- Stockwell, R. G., L. Mansinha, and R. P. Lowe (1996). Localization of the complex spectrum: The S transform, *IEEE Trans. Signal Process.* **44**, no. 4, 998–1001.
- Stutzmann, E., F. Ardhuin, M. Schimmel, A. Mangeney, and G. Patau (2012). Modelling long-term seismic noise in various environments, *Geophys. J. Int.* **191**, no. 2, 707–722.
- Sun, B., J. Ma, H. Chauris, and H. Yang (2009). Solving wave equations in the curvelet domain: A multi-scale and multi-directional approach, *J. Seismic Explor.* **18**, no. 4, 385–399.
- Tang, G., and J. Ma (2010). Application of total-variation-based curvelet shrinkage for three-dimensional seismic data denoising, *IEEE Geosci. Remote Sens. Lett.* **8**, no. 1, 103–107.
- Turner, G. (1990). Aliasing in the tau-p transform and the removal of spatially aliased coherent noise, *Geophysics* **55**, no. 11, 1496–1503.
- Weaver, J. B., Y. Xu, D. M. Healy Jr., and L. D. Cromwell (1991). Filtering noise from images with wavelet transforms, *Magn. Reson. Med.* **21**, no. 2, 288–295.
- White, R. E. (1988). Maximum kurtosis phase correction, *Geophys. J. Int.* **95**, no. 2, 371–389.
- Yang, H., and L. Zhu (2010). Shallow low-velocity zone of the San Jacinto fault from local earthquake waveform modelling, *Geophys. J. Int.* **183**, no. 1, 421–432.
- Yang, H., Y. Duan, J. Song, X. Jiang, X. Tian, W. Yang, W. Wang, and J. Yang (2020). Fine structure of the Chenghai fault zone, Yunnan, China, constrained from teleseismic travel time and ambient noise tomography, *J. Geophys. Res.* **125**, no. 7, e2020JB019565, doi: [10.1029/2020JB019565](https://doi.org/10.1029/2020JB019565).
- Yang, H., Z. Li, Z. Peng, Y. Ben-Zion, and F. Vernon (2014). Low-velocity zones along the San Jacinto fault, southern California, from body waves recorded in dense linear arrays, *J. Geophys. Res.* **119**, no. 12, 8976–8990.
- Yang, Y., C. Liu, and C. A. Langston (2020). Processing seismic ambient noise data with the continuous wavelet transform to obtain reliable empirical Green's functions, *Geophys. J. Int.* **222**, no. 2, 1224–1235.
- Yilmaz, Ö. (2001). Seismic data analysis: Processing, inversion, and interpretation of seismic data, *Society of Exploration Geophysicists*, San Antonio, 09–14 September 2001.
- Zhan, Z., Q. Li, and J. Huang (2018). Application of wavefield compressive sensing in surface wave tomography, *Geophys. J. Int.* **213**, no. 3, 1731–1743.
- Zhang, J., and C. A. Langston (2020). Separating the scattered wavefield from teleseismic P using curvelets on the Long Beach array data set, *Geophys. J. Int.* **220**, no. 2, 1112–1127.
- Zhang, J., and C. A. Langston (2022). Teleseismic P-to-Rayleigh conversions from near-surface geological structure along the Newport–Inglewood fault zone in Long Beach, California, *Bull. Seismol. Soc. Am.* **112**, no. 3, 1356–1372.
- Zhong, T., Y. Li, N. Wu, P. Nie, and B. Yang (2015). Statistical analysis of background noise in seismic prospecting, *Geophys. Prospect.* **63**, no. 5, 1161–1174.
- Zhu, L., and L. A. Rivera (2002). A note on the dynamic and static displacements from a point source in multilayered media, *Geophys. J. Int.* **148**, no. 3, 619–627.

Manuscript received 23 February 2024

Published online 21 June 2024